Near-field focusing with optical phase antennas

A. G. Curto,[1] A. Manjavacas,[2] and F. J. García de Abajo[2,*]

[1] *ICFO Institut de Ciencies Fotoniques, Mediterranean Technology Park, 08860, Castelldefels (Barcelona), Spain*

[2] *Instituto de Óptica - CSIC and Unidad Asociada CSIC-Universidade de Vigo, Serrano 121, 28006 Madrid, Spain*

[*] *Corresponding author: jga@cfmac.csic.es*

Abstract: We investigate the near-field focusing properties of three-dimensional phase antennas consisting of concentric rings designed to have source and image spots separated by several microns from the lens. Tight focal spots are obtained for silicon or gold rings patterned in a silica matrix. We analyze in detail the dependence of the performance of these lenses on geometrical parameters such as the number of rings, the ring thickness, and the focal distance. Subwavelength focal spots are found to form at distances of tens of wavelengths from the lens, thus suggesting applications to remote sensing and penlight microscopy and lithography.

OCIS codes: (290.5870) Rayleigh scattering; (050.1950) Diffraction gratings.

References and links

1. H. Xu, E. J. Bjerneld, M. Käll, and L. Börjesson, "Spectroscopy of single hemoglobin molecules by surface enhanced Raman scattering," Phys. Rev. Lett. **83**, 4357–4360 (1999).
2. S. I. Bozhevolnyi, V. S. Volkov, E. Devaux, J. Y. Laluet, and T. W. Ebbesen, "Channel plasmon subwavelength waveguide components including interferometers and ring resonators," Nature **440**, 508–511 (2006).
3. K. Kneipp, Y. Wang, H. Kneipp, L. T. Perelman, I. Itzkan, R. R. Dasari, and M. S. Feld, "Single molecule detection using surface-enhanced Raman scattering (SERS)," Phys. Rev. Lett. **78**, 1667–1670 (1997).
4. S. Nie and S. R. Emory, "Probing single molecules and single nanoparticles by surface-enhanced Raman scattering," Science **275**, 1102–1106 (1997).
5. L. Rodríguez-Lorenzo, R. A. Álvarez-Puebla, I. Pastoriza-Santos, S. Mazzucco, O. Stéphan, M. Kociak, L. M. Liz-Marzán, and F. J. García de Abajo, "Zeptomol Detection through controlled ultrasensitive surface-enhanced Raman scattering," J. Am. Chem. Soc. **131**, 4616–4618 (2009).
6. H. Shi, C. Wang, C. Du, X. Luo, X. Dong, and H. Gao, "Beam manipulating by metallic nano-slits with variant widths," Opt. Express **13**, 6815–6820 (2005).
7. F. M. Huang, N. Zheludev, Y. Chen, and F. J. García de Abajo, "Focusing of light by a nano-hole array," Appl. Phys. Lett. **90**, 091,119 (2007).
8. T. Xu, C. Du, C. Wang, and X. Luo, "Subwavelength imaging by metallic slab lens with nanoslits," Appl. Phys. Lett. **91**, 201,501 (2007).
9. M. R. Dennis, N. I. Zheludev, and F. J. García de Abajo, "The plasmon Talbot effect," Opt. Express **15**, 9692–9700 (2007).
10. A. G. Curto and F. J. García de Abajo, "Near-field optical phase antennas for long-range plasmon coupling," Nano Lett. **8**, 2479–2484 (2008).
11. E. Schonbrun, C. Rinzler, and K. B. Crozier, "Microfabricated water immersion zone plate optical tweezer," Appl. Phys. Lett. **92**, 071,112 (2008).
12. L. Markley, A. M. H. Wong, Y. Wang, and G. V. Eleftheriades, "Spatially shifted beam approach to subwavelength focusing," Phys. Rev. Lett. **101**, 113,901 (2008).
13. F. M. Huang and N. I. Zheludev, "Super-resolution without evanescent waves," Nano Lett. **9**, 1249–1254 (2009).
14. A. A. Maradudin and T. A. Leskova, "The Talbot effect for a surface plasmon polariton," New J. Phys. **11**, 033,004 (2009).

#115076 - $15.00 USD Received 30 Jul 2009; accepted 30 Aug 2009; published 18 Sep 2009

15. L. Verslegers, P. B. Catrysse, Z. Yu, J. S. White, E. S. Barnard, M. L. Brongersma, and S. Fan, "Planar lenses based on nanoscale slit arrays in a metallic film," Nano Lett. **9**, 235–238 (2009).
16. H. F. Talbot, "Facts relating to optical science, No. IV," Philos. Mag. **9**, 401–407 (1836).
17. M. V. Berry and S. Klein, "Integer, fractional and fractal Talbot effects," J. Mod. Opt. **43**, 2139–2164 (1996).
18. W. Chao, B. D. Harteneck, J. A. Liddle, E. H. Anderson, and D. T. Attwood, "Soft X-ray microscopy at a spatial resolution better than 15 nm," Nature **435**, 1210–1213 (2005).
19. F. J. García de Abajo and A. Howie, "Retarded field calculation of electron energy loss in inhomogeneous dielectrics," Phys. Rev. B **65**, 115,418 (2002).
20. E. M. Purcell and C. R. Pennypacker, "Scattering and absorption of light by nonspherical dielectric grains," Astrophys. J. **186**, 705–714 (1973).
21. B. T. Draine and P. J. Flatau, "Discrete-dipole approximation for scattering calculations," J. Opt. Soc. Am. A **11**, 1491–1499 (1994).
22. F. J. García de Abajo, A. Rivacoba, N. Zabala, and P. M. Echenique, "Electron energy loss spectroscopy as a probe of two-dimensional photonic crystals," Phys. Rev. B **68**, 205,105 (2003).
23. M. V. Berry and E. Bodenschatz, "Caustics, multiply reconstructed by Talbot interference," J. Mod. Opt. **46**, 349–365 (1999).

1. Introduction

The ability to focus light within tiny spaces is important for applications as diverse as molecule sensing [1] and signal processing [2]. In this context, several schemes have been devised to manipulate the near field, leading to dramatic enhancement of the light intensity, which can reach 10^5 levels in the vicinity of plasmon-supporting metallic nanostructures, as deduced from surface-enhanced Raman scattering (SERS) measurements [3, 4, 5]. A different approach towards light concentration is being currently explored, based upon constructive interference of diffracted waves in the near- and intermediate-field regimes [6, 7, 8, 9, 10, 11, 12, 13, 14, 15]. For example, phase antennas have been engineered to superimpose propagating scattered plasmon waves in order to achieve strong coupling between physically-separated localized plasmons [10]. Plasmon interference has also been realized to produce self-imaging of periodic structures [9, 14], similar to the Talbot effect observed in freely propagating light after transmission through a grating [16, 17]. In independent developments, the constructive interference of light transmitted through slits of varying width [6, 12, 15] and quasi-crystalline distributions of holes [7] has been used to produce near-field focusing of a plane wave. Remarkably, this principle has been recently employed to demonstrate optical tweezing using a Fresnel zone plate [11].

We investigate here the ability of phase antennas to concentrate light in three dimensional space when operating over regions spanning a few light wavelengths. More precisely, we present a three-dimensional implementation of a near-field lens that is designed to focus a point source on an image spot separated by several wavelengths. A scheme of the lens is shown in Fig. 1. A source dipole is taken to be positioned at one of the two focal spots of the lens (point S). An image spot is formed in the other focus, situated in the far side of the lens (point I). The lens consists of an arrangement of concentric rings, the radii of which are chosen so that the lengths of the geometrical paths emerging from S, scattered by consecutive rings, and refocused in I differ by an optical wavelength $\lambda = \lambda_0/n$, where n is the index of refraction of the embedding medium ($n = 1.45$ in silica at a vacuum wavelength $\lambda_0 = 1550\,\mathrm{nm}$). The radii deduced from this geometrical condition satisfy the relation

$$b_i = \sqrt{(i\lambda/2)^2 - a^2} \qquad (|i| \geq 2a/\lambda), \tag{1}$$

where the distance from the lens plane to the source and image points is considered to have the same value a for simplicity, and the integer i labels different rings. The actual size of the image spot is shown in Fig. 1 for 15 silicon rings surrounded by silica, with $a = 10\lambda = 10.7\,\mu\mathrm{m}$ and a ring inner radius of $R = 100\,\mathrm{nm}$. This type of design is related to Fresnel lenses, which

#115076 - $15.00 USD Received 30 Jul 2009; accepted 30 Aug 2009; published 18 Sep 2009

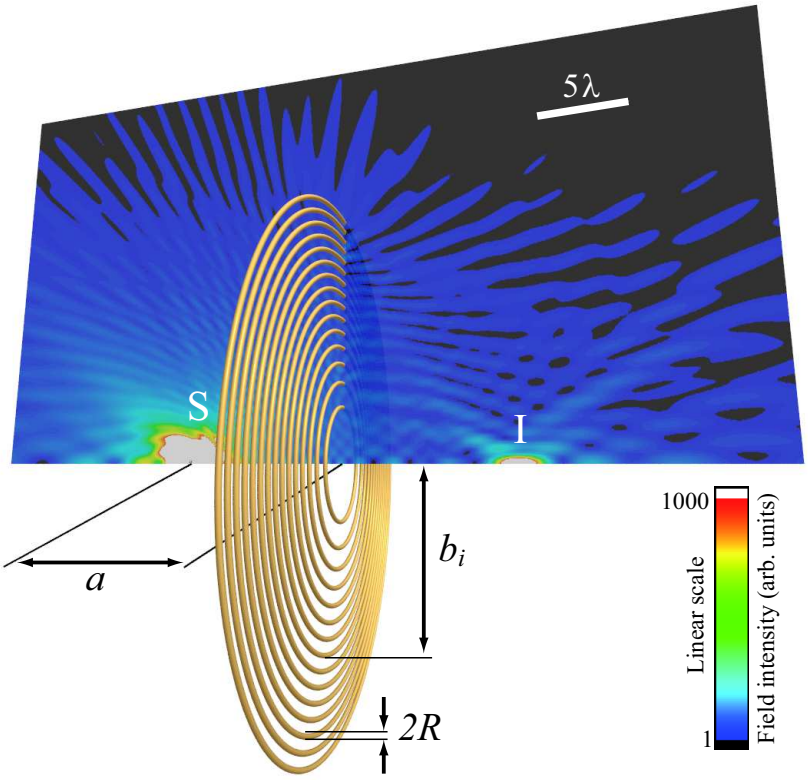

Fig. 1. Near-field lens and example of focusing. The lens is formed by $N = 15$ coplanar, concentric silicon nanowires embedded in silica ($n = 1.45$), and it is designed to focus a point source S on an image spot I. For simplicity we consider both image and source to be equally separated at a distance $a = 10\lambda$ from the plane of the rings. The free-space wavelength is $\lambda_0 = 1550\,\text{nm}$. The rings have inner radius $R = 100\,\text{nm}$ and external radii b_n determined by the condition of constructive interference (see Eq. (1)). The bar scale in the figure is given relative to the wavelength inside the silica, $\lambda = \lambda_0/n$. The source is an electric dipole of magnitude $\mathbf{P}^{\text{ext}} = \hat{\mathbf{x}} + \mathrm{i}\hat{\mathbf{y}}$.

#115076 - $15.00 USD Received 30 Jul 2009; accepted 30 Aug 2009; published 18 Sep 2009

have become so useful to focus x rays [18], but with the rings occupying narrow regions of nearly-zero phase, rather than blocking wider regions of negative phase. We explore here the performance of these lenses when the thickness of the rings are in the nanoscale and the operating wavelengths in the near infrared. In the particular design of Fig. 1, we have calculated the fraction of power emitted from the source dipole that is passing through the source focal spot within the circle defined by the HWHM distance to be 0.7%. As one of our main conclusions, we anticipate that the quality of the image focal spot is remarkably good in our scheme, compared to other light focusing approaches.

The image field should grow logarithmically with the number of rings N, as demonstrated by the following simple argument: the source field decays as the inverse of the distance for large separations from the emitting point dipole at S (this distance is $1/(i\lambda/2)$ for the ring i); similarly, the on-axis field produced by a uniformly-polarized ring decays with the distance to the ring times its length $2\pi b_i$ (this factor accounts for an effective distribution of induced dipoles along the length of the ring circumference); each ring i is thus contributing to the image with a field proportional to $b_i/(i\lambda/2)^2$, so that the overall in-phase field scales as

$$\sum_i \frac{b_i}{(i\lambda/2)^2} \propto \log(N) \tag{2}$$

for large N. The field enhancement at the image spot is clearly resolved in Fig. 1.

The near-field intensity plotted in Fig. 1 has been obtained by rigorously solving Maxwell's equations using the boundary element method (BEM) [19] in an implementation specifically designed to deal with axially-symmetric objects. In the BEM, the electromagnetic fields are expressed in terms of boundary charges and currents distributed on the surfaces of the rings. These boundary sources are self-consistently obtained by using the customary boundary conditions for the electromagnetic field, leading to a system of equations that involves integrals over the ring surfaces. We solve these equations upon discretization of the integrals, thus transforming the problem into a set of linear equations. The surface integrals are recast into contour integrals when the axial symmetry of the rings is taken into consideration, so that only 100 points per ring are sufficient to achieve convergence. Further details on the method can be found in Ref. [19].

The remainder of this paper is devoted to studying the dependence of the performance of this type of lens on geometrical and compositional parameters. A simple analytical model, which should be exact in the limit of very thin wires, is first formulated, allowing us to understand the process of image formation as originating in dipole polarization of the rings. We conclude with a brief discussion of possible applications of near-field lenses.

2. Analytical model

Further insight into the image formation process can be gained from an analytical model that is valid for thin rings ($R \ll \lambda$). The nano-rings considered here to form the near-field lens have inner radius much smaller than the wavelength but external radius comparable or larger than the wavelength. Therefore, the electromagnetic response of these structures can be approximately expressed in terms of the scattering properties of a straight thin wire of infinite extension, and in particular, the dipolar components of this scattering should be dominant in the limit of thin wires. Next, we elaborate this idea and obtain a simple analytical model that compares reasonably well with the full solution of Maxwell's equations for the actual lens.

The response of each ring i in the lens is represented by an effective polarization per unit length $\mathbf{P}_i$ having radial, azimuthal, and longitudinal components with respect to the ring circumference and the lens axis (i.e., along directions $\hat{\mathbf{R}}$, $\hat{\boldsymbol{\varphi}}$, and $\hat{\mathbf{z}}$, respectively, with the axis of rotational symmetry oriented along z).

#115076 - $15.00 USD Received 30 Jul 2009; accepted 30 Aug 2009; published 18 Sep 2009

The induced dipoles satisfy a self-consistent equation that is formally equivalent to the discrete-dipole approximation formula [20, 21],

$$\mathbf{P}_i = \alpha_i \left[\mathbf{E}_i^{\text{ext}} + \sum_{j \neq i} G_{ij} \mathbf{P}_j \right], \tag{3}$$

where α_i is the polarizability per unit length in ring i, and the 3×3 matrix G_{ij} is used to obtain the electric field produced at ring i by the polarization of ring j. The latter is given by the integral of the point-dipole field over the circumference of ring j,

$$G_{ij,ab} = b_j \int d\varphi \, \left[k^2 \, \hat{\mathbf{u}}_a^0 \cdot \hat{\mathbf{u}}_b^\varphi + (\hat{\mathbf{u}}_a^0 \cdot \nabla)(\hat{\mathbf{u}}_b^\varphi \cdot \nabla) \right] \frac{\mathrm{e}^{\mathrm{i}k|\mathbf{r}_i^0 - \mathbf{r}_j^\varphi|}}{|\mathbf{r}_i^0 - \mathbf{r}_j^\varphi|} \, \mathrm{e}^{\mathrm{i}\varphi}, \tag{4}$$

where $k = 2\pi/\lambda$ is the light wavevector inside the host material; the superscripts a and b run over cylindrical directions $\hat{\mathbf{u}}_b^\varphi \in \left\{ \hat{\mathbf{R}}, \hat{\varphi}, \hat{\mathbf{z}} \right\}$ (notice that both $\hat{\mathbf{R}} = \hat{\mathbf{x}} \cos\varphi + \hat{\mathbf{y}} \sin\varphi$ and $\hat{\varphi} = -\hat{\mathbf{x}} \sin\varphi + \hat{\mathbf{y}} \cos\varphi$ depend upon the azimuthal angle φ); the integral is taken over the points $\mathbf{r}_j^\varphi = b_j \hat{\mathbf{R}}$ along the circumference of ring j; and a single representative point of ring i is selected, $\mathbf{r}_i^0 = b_i \hat{\mathbf{x}}$.

The external source is taken to be a dipole of magnitude

$$\mathbf{P}^{\text{ext}} = \hat{\mathbf{x}} + \mathrm{i}\hat{\mathbf{y}} = (\hat{\mathbf{R}} + \mathrm{i}\hat{\varphi}) \mathrm{e}^{\mathrm{i}\varphi}, \tag{5}$$

so that the components of the external field acting on the representative point of ring i become $E_{i,R}^{\text{ext}} = A - B b_i^2 / d_i^2$, $E_{i,\varphi}^{\text{ext}} = \mathrm{i}A$, and $E_{i,z}^{\text{ext}} = -B b_i a / d_i^2$, where $A = [(kd_i)^2 + \mathrm{i}kd_i - 1]\mathrm{e}^{\mathrm{i}kd_i}/d_i^3$, $B = [(kd_i)^2 + 3\mathrm{i}kd_i - 3]\mathrm{e}^{\mathrm{i}kd_i}/d_i^3$, and $d_i = i\lambda/2$ is the distance from the source to the ring circumference. The $\mathrm{e}^{\mathrm{i}\varphi}$ factor in Eq. (5) indicates that the problem has $m = 1$ overall azimuthal symmetry. This factor is directly translated into the integrand of Eq. (4), which already includes this azimuthal dependence of the polarization.

We have so far considered that each ring responds though a polarization per unit length along its circumference, $(P_{iR}\hat{\mathbf{R}} + P_{i\varphi}\hat{\varphi} + P_{iz}\hat{\mathbf{z}})\mathrm{e}^{\mathrm{i}\varphi}$. Now, we can make a simplifying assumption by assuming long rings of radii $b_i \gg \lambda$. Then, the response can be considered to be locally equivalent to that of an infinite cylinder oriented along the ring tangent. It should be noted that the response of such cylinder can be naturally decomposed into components of fixed wavevector q along the cylinder axis ξ, yielding a spatial dependence $\exp(\mathrm{i}q\xi)$. This is to be compared with $\mathrm{e}^{\mathrm{i}\varphi}$ in Eq. (5), so that we can assimilate $\xi = b_i\varphi$ and take $q = 1/b_i$ for the ring i. With the notation and methods of Ref. [22], and considering the implicit definition of $\mathbf{P}_i$ in Eq. (3), the polarizability reduces to $\alpha_{i,R} = \alpha_{i,z} = -2\mathrm{i}t_{1,ss}/\pi k^2$ and $\alpha_{i,\varphi} = -\mathrm{i}t_{0,pp}/\pi Q^2$, where $Q = \sqrt{k^2 - q^2}$, and $t_{1,ss}$ and $t_{0,pp}$ are dipolar elements of the cylinder scattering matrix.

The analytical model for a lens consisting of N rings requires to solve Eq. (3), that is, a system of $3N$ equations with $3N$ variables (all 3 components of all N polarization vectors), which is much faster than the rigorous solution computed with BEM.

The result of this analytical approach is represented in Fig. 2(a) under the same conditions as in Fig. 1. The main characteristics of the near-field distribution are in reasonable agreement with the full solution of Maxwell's equations for the same system (Fig. 2(b)). In particular, the relative intensity of the image spot is similar in both analytical and fully-numerical calculations. Even the positions of intensity maxima near the lens and their extension away from the lens are very similar in both calculations. This is consistent with the fact that the rings inner radius is much smaller than the wavelength, so that the dipolar part of their response is dominant. The validity of this model constitutes a solid proof of the scaling of the image-spot logarithmic divergence with the number of rings N (see Eq. (2)), which stems from pure geometrical

#115076 - $15.00 USD Received 30 Jul 2009; accepted 30 Aug 2009; published 18 Sep 2009

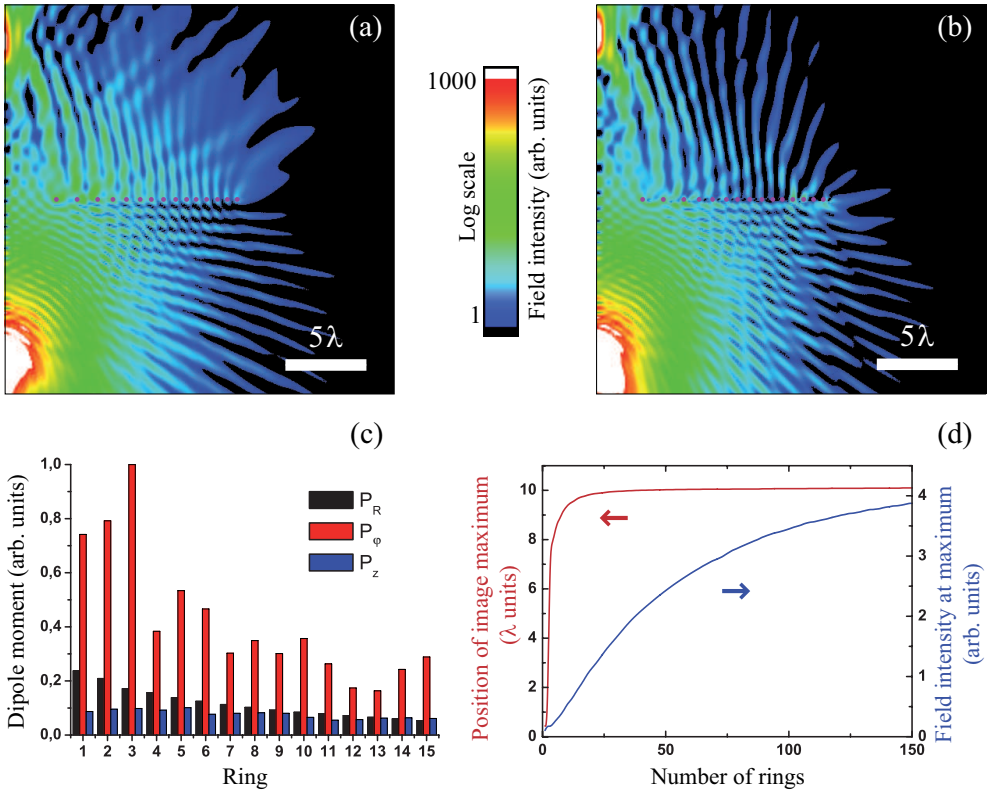

Fig. 2. Comparison between (a) a semi-analytical model (see Sec. 2) and (b) the full solution of Maxwell's equations using BEM under the same conditions as in Fig. 1 (i.e., $N = 15$ silicon rings of radius $R = 100$ nm embedded in silica and a free-space wavelength $\lambda_0 = 1550$ nm). The plane of representation and the source dipole are the same as in Fig. 1 and the rings are shown as pink solid circles. The strength of the induced-polarization components along radial ($|P_R|$), azimuthal (out-of-plane, $|P_\varphi|$), and rotational-axis ($|P_z|$) directions is shown in (c) for each of the rings (1 =innermost, 15 =outermost). The evolution of the position and field intensity at the image spot maximum with the number of rings is shown in (d). Both (c) and (d) are calculated with the analytical model.

arguments and the assumption that the rings respond as effective dipoles distributed along their circumference. Figure 2(d) shows the field intensity at the image spot maximum as a function of N, showing the expected logarithmic dependence. Interestingly, the position of the spot maximum, also shown in the figure, is rapidly converging towards a value close to the geometrical focus ($a = 10\lambda$), which is reached for $N > 25$.

This model allows us to easily explore the role of different rings in the image formation process. Figure 2(c) shows the strength of the different cylindrical components of the polarization vector for each ring in the lens, labeled 1 to 15 from the innermost ring to the outermost one. The plot demonstrates that the azimuthal polarization component is dominant, and it is maximum near the lens center, although outer rings are also contributing significantly, particularly when considering that the total polarization is amplified there when multiplying by a larger circumference length.

#115076 - $15.00 USD Received 30 Jul 2009; accepted 30 Aug 2009; published 18 Sep 2009

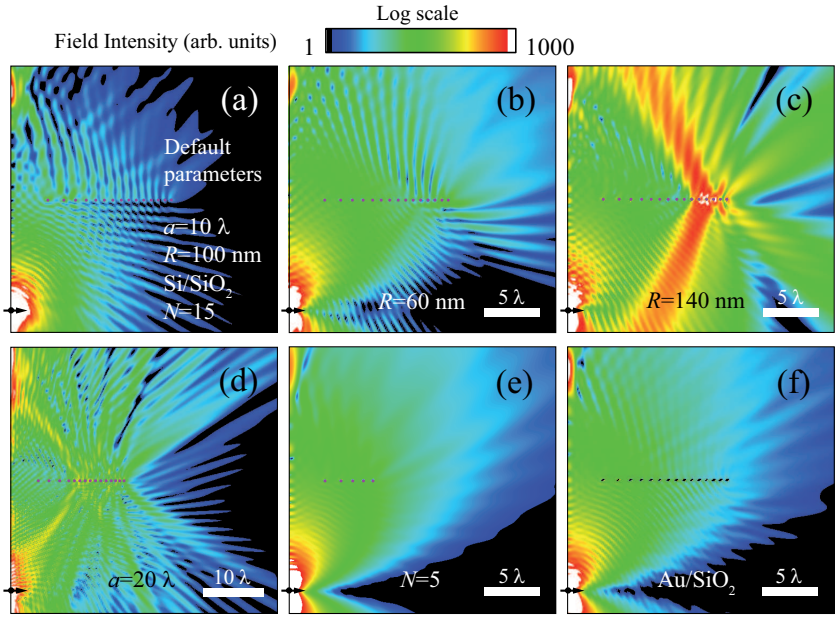

Fig. 3. Variation of the lens performance with geometrical and compositional parameters calculated from BEM. The default parameters given in (a) are the same as in Fig. 1, and each of the panels (b)-(f) shows the field intensity when one of these parameters is varied, as indicated by text insets. (b),(c): Variation with ring inner radius R. (d): Variation with focal distance a. (e) Variation with number of rings N. (f) Variation with material in the rings. The source is an electric dipole $\mathbf{P}^{\text{ext}} = \hat{\mathbf{x}}$, as shown by black arrows, and the free-space wavelength is $\lambda_0 = 1550\,\text{nm}$. The plane of representation is the same as in Fig. 1 in all cases.

3. Performance of near-field phase antennas

Figure 3 presents overviews of the near field in a region encompassing the lens and its two focal spots for different variations of the lens parameters, all of them obtained from a rigorous solution of Maxwell's equations using BEM for a source dipole $\mathbf{P}^{\text{ext}} = \hat{\mathbf{x}}$. Fig. 3(a) shows results for default parameters that are then varied in Figs. 3(b)-(f), as indicated by text insets. In general terms, the image focal spot becomes weaker when reducing the thickness of the rings (Fig. 3(b)) or when decreasing its number (Fig. 3(e)), in accordance with the prediction of Eq. (2). In contrast, the image intensity grows for thicker rings (Fig. 3(c)) and it becomes more complex, acquiring some internal structure, when increasing the focal distance (Fig. 3(d)). Furthermore, the focusing ability of the lens does not seem to depend critically on the ring material (cf. Fig. 3(f) for gold and Fig. 3(a) for silicon).

The quality of the image focal spot and its dependence on geometrical parameters is studied in Fig. 4. The focus has subwavelength diameter in the radial direction but it is elongated along the lens axis. The focus dimensions for a combination of inner ring radius $R = 100\,\text{nm}$ and focal distance $a = 10.7\,\mu\text{m}$ are typical of a regular objective with FWHM$= 0.76\lambda$, although FWHM$= 0.50\lambda$ is possible when 300 rings are added to the lens (not shown). Actually, the focal spot is narrower in the direction perpendicular to both the plane of the figure and the source dipole (not shown), yielding FWHM$= 0.51$ for 15 rings. It should be noted that the geometrical

#115076 - $15.00 USD Received 30 Jul 2009; accepted 30 Aug 2009; published 18 Sep 2009

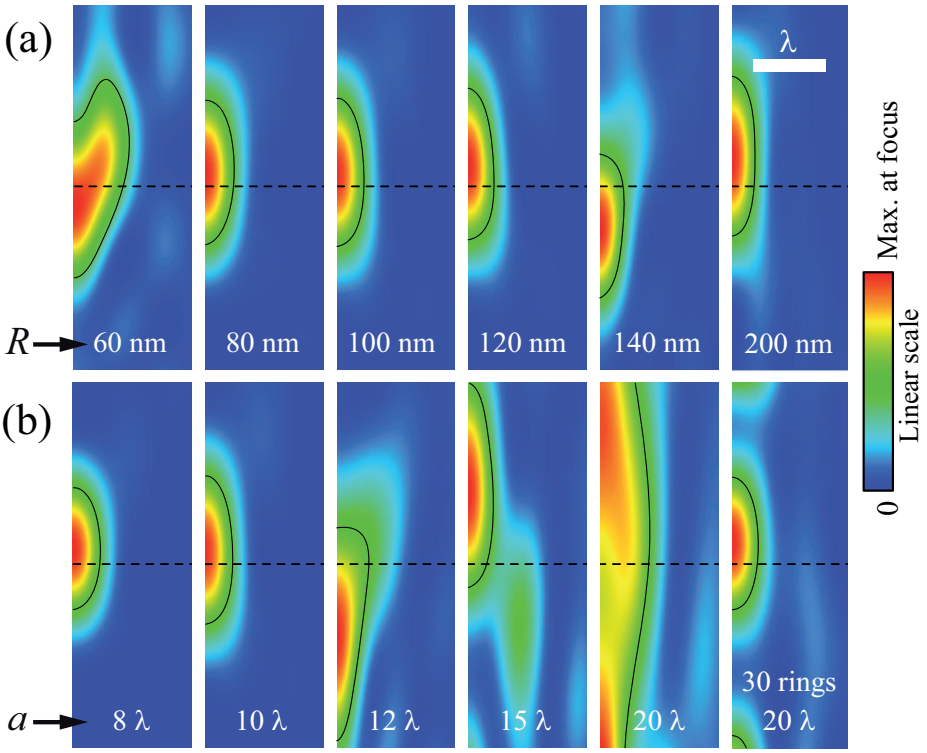

Fig. 4. Dependence of the lens focusing properties on (a) the inner radius of the rings R (for $a = 10\lambda$) and (b) the focal distance a (for $R = 100$ nm), calculated using BEM. The lens is made of $N = 15$ silicon rings in a silica matrix, except the lower-right plot, calculated for 30 rings. The plots are close-ups of the image spot intensity in the same plane of representation as in Fig. 1, but the source is a dipole $\mathbf{P}^{\text{ext}} = \hat{\mathbf{x}}$. The intensity is given in linear scale and normalized to its maximum in each plot. The contour of half-maximum intensity is shown as solid lines. The geometrical focus is indicated by dashed lines.

condition expressed in Eq. (1) assumes idealized line-like rings, but in fact, the optimum inner ring radius seems to be above 80-100 nm, which is approximately a tenth of the wavelength inside the silica host material, and even for $R = 140$ nm the focal spot is relatively narrow. The actual position of the focus oscillates around the geometric optics focus when changing R, partly as a result of multiple scattering among the rings and also because of deviations from ray optics similar to those noted in nonparaxial discussions of the Talbot effect [9, 23]. It is also possible that the number of rings considered in Fig. 4 is still below the saturation level for the position of the image maximum with increasing N, as observed in Fig. 2(d) for $N < 25$. The focus is more degraded when the lens is designed for larger focal distances (Fig. 4(b)) with a constant number of rings ($N = 15$), but image focal spots of good quality are recovered when the number of rings is increased in proportion to a, as shown in the lower-right plot of Fig. 4(b) ($N = 30$).

A lens designed to operate at fixed wavelength $\lambda_{0,ref}$ can still work at wavelengths close to that value, although chromatic dispersion will spoil the image focus, as illustrated in Fig. 5. This figure shows that relatively good focusing is still achieved at wavelengths within a range of ± 10 nm with respect to $\lambda_{0,ref} = 1550$ nm. This narrow spectral response of the lens antenna

#115076 - $15.00 USD Received 30 Jul 2009; accepted 30 Aug 2009; published 18 Sep 2009

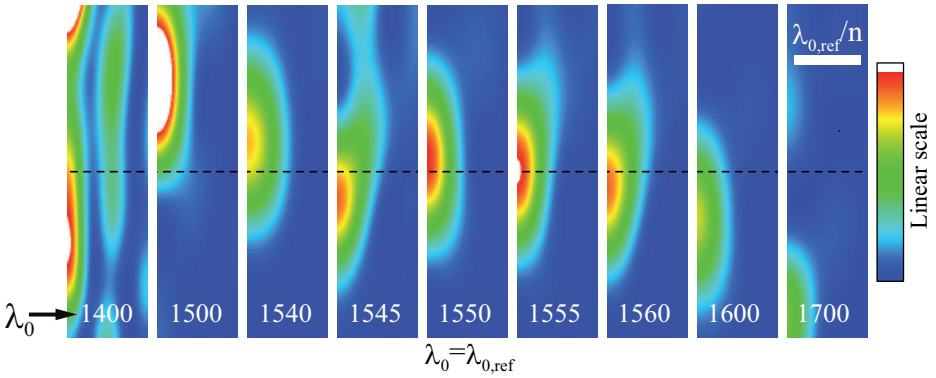

Fig. 5. Chromatic dispersion of the antenna of Fig. 1, designed for a free-space wavelength $\lambda_{0,ref} = 1550\,\text{nm}$, but operating at different vacuum wavelengths λ_0, as indicated in each plot. The dashed line indicates the geometrical focus position $z = a$. The intensity is calculated using BEM, normalized to the maximum for $\lambda_0 = \lambda_{0,ref}$, and represented in linear scale. The plane of representation is the same as in Fig. 1, but the source is a dipole $\mathbf{P}^{\text{ext}} = \hat{\mathbf{x}}$.

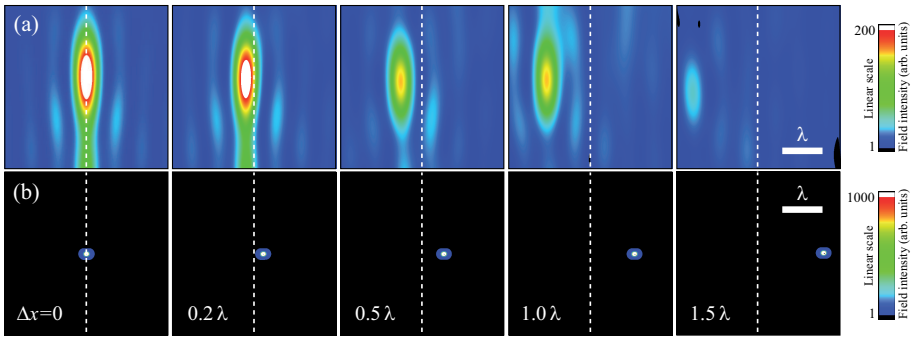

Fig. 6. Focusing of off-axis spots. The lower images (b) show different source spots, laterally displaced away from the axis of the lens by a distance Δx as indicated by labels. The upper images (a) show the corresponding image spots. The vertical dashed lines indicate the lens axis. The antenna has 30 silicon rings embedded in silica and a focal distance of 10λ. The free-space light wavelength is $\lambda_0 = 1550\,\text{nm}$. The external dipole is like in Eq. (5).

can be advantageous to filter specific wavelengths.

The focusing properties of the lens for off-axis point sources are explored in Fig. 6. Like in a regular lens, the image spot is displaced laterally in the direction opposite to the source spot. The lens is capable of rendering well-defined image spots with 1:1 scaling up to displacements of the order of the light wavelength. This can be important for imaging without distortion extended objects distributed in a plane.

We have so far considered symmetric lenses. However, the rings in the lens can be designed to have different source (a_1) and image (a_2) focal distances simply by changing Eq. (1) to $\sqrt{a_1^2+b_i^2}+\sqrt{a_2^2+b_i^2} = i\lambda + C$. This situation is considered in Fig. 7, in which the constant C is chosen such that the inner ring has a radius independent of a_2 and determined by Eq.

#115076 - $15.00 USD Received 30 Jul 2009; accepted 30 Aug 2009; published 18 Sep 2009

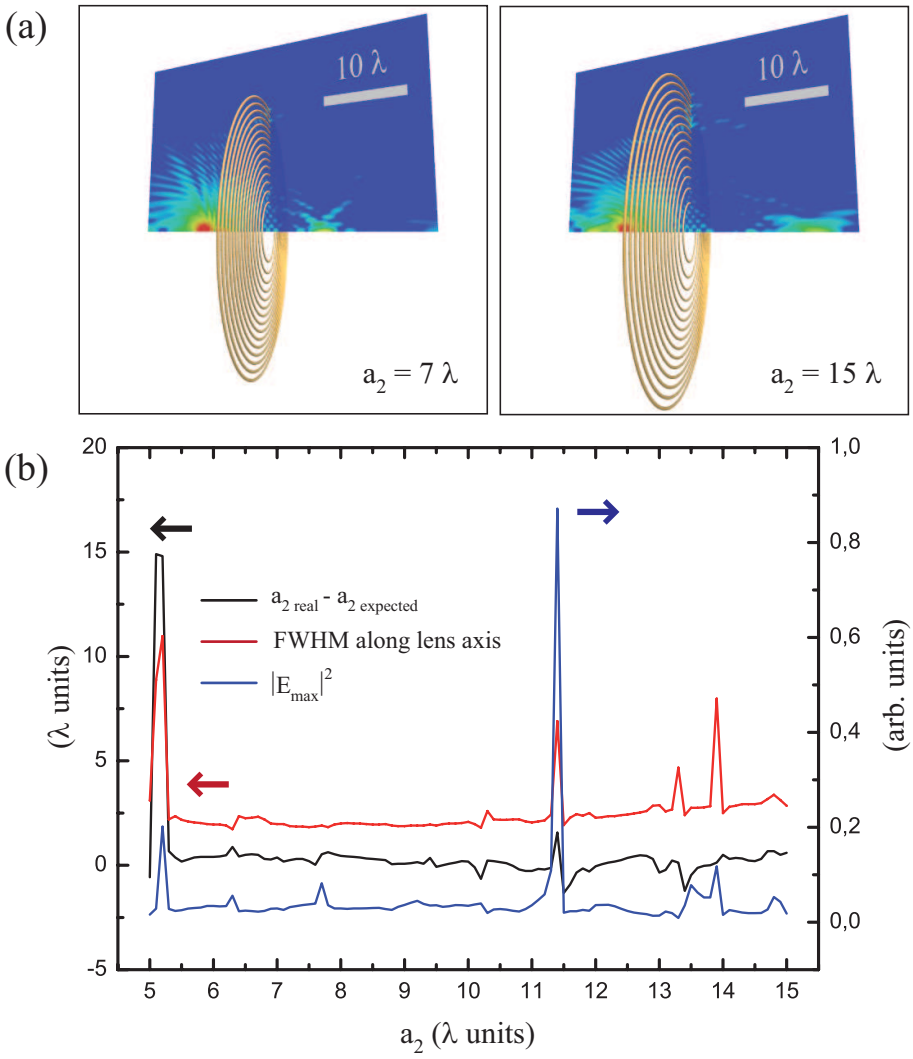

Fig. 7. Lens focusing for different source and image focal distances. The source focal distance is fixed at $a_1 = 10\lambda$. The near-field distribution is represented in (a) for two different values of the image focal distance a_2. Some basic parameters describing the image spot are represented in (b) as a function of a_2: the actual position of the image spot maximum relative to a_2 (black curve), the FWHM of the spot along the lens axis direction (red curve), and the electric field intensity maximum (blue curve). The number of rings (silicon on silica) is maintained fixed at $N = 15$. The light wavelength is $\lambda_0 = 1550$nm. The external dipole is like in Eq. (5). A video showing the evolution of the near field intensity as the image focal distance is varied is available at Media 1.

#115076 - $15.00 USD Received 30 Jul 2009; accepted 30 Aug 2009; published 18 Sep 2009

(1) (i.e., $C = 0$ for $a_1 = a_2$). In particular, Fig. 7(a) clearly shows well-defined image spots in the near-field distributions for two different values of a_2 and fixed value of $a_1 = 10\lambda$. The actual position of the image spot evolves slightly around the design value a_2 as we move this parameter [see Fig. 7(b), black curve]. Like in our case, this type of effect is familiar in non-paraxial configurations, as previously reported in the plasmon Talbot effect [9]. The FWHM of the image spot along the lens axis [Fig. 7(b), red curve] stays rather constant, except for a slight increase with a_2, which we attribute to the finite, fixed number of rings ($N = 15$) considered in Fig. 7. (The transversal FWHM is mostly within the $0.5\lambda - 0.6\lambda$ range for the values of a_2 under consideration.) Interestingly, these parameters show large variations at $a_2 \approx 5.2\lambda$ and $a_2 \approx 11.4\lambda$, which are accompanied by a significant increase in the maximum electric field intensity at the source spot [Fig. 7(b), blue curve]. These are the signatures of resonant modes involving the entire lens, similar to Mie modes in large dielectric spheres. Incidentally, the reciprocity theorem guarantees that the intensity would go through a dip if the source and image focal distances are interchanged. Therefore, the dips observed in the field intensity of Fig. 7(b) are also related to lens resonances.

4. Concluding remarks

The near-field lenses that we discuss here should be easy to fabricate using standard lithography or imprinting techniques. Although we have studied for simplicity the symmetric case, with both source and image spots positioned in the same host material, these concepts can be easily generalized to lenses with two different focal distances, a_1 and a_2, in an asymmetric environment of dielectrics with indices n_1 and n_2, leading to ring radii b_i satisfying the equation

$$n_1\sqrt{a_1^2+b_i^2}+n_2\sqrt{a_2^2+b_i^2}=i\lambda_0. \tag{6}$$

In particular, a lens could be patterned on a glass surface to communicate a focal spot inside the glass (or even on the other surface of the glass if it is a film) with a focal spot in the surrounding medium (e.g., a fluid or air).

Another situation of practical interest is presented when a very distant source is considered, so that the lens is capable of focusing an incident plane wave under the condition $b_i = \sqrt{(i\lambda)^2 - a^2}$. This is similar to a Fresnel lens.

Near-field antennas can be advantageous in pen-light reading and writing because they are flat, which facilitates its integration in movable parts (e.g., sensors). The remarkable quality of the image focal spot in our simulations can be advantageous for exploiting ring-based phase antennas in these types of applications. The ability to sense an optical signal at a source spot and detect it at an image spot separated by tens of microns can find practical use for sensing minute concentrations of molecules by scanning the surface or volume on which they are distributed.

Acknowledgments

This work has been supported by the Spanish MICINN (MAT2007-66050 and Consolider NanoLight.es) and by the EU (NMP4-2006-016881-SPANS and NMP4-SL-2008-213669-ENSEMBLE).

#115076 - $15.00 USD Received 30 Jul 2009; accepted 30 Aug 2009; published 18 Sep 2009